Front. Mech. Eng. 2019, 14(3): 255–272
https://doi.org/10.1007/s11465-019-0538-x

RESEARCH ARTICLE

Chengyuan LIANG, Fang YUAN, Xuedong CHEN, Wei JIANG, Lizhan ZENG, Xin LUO

Comprehensive analysis of the influence of structural and dynamic parameters on the accuracy of nano-precision positioning stages

Abstract Nano-precision positioning stages are characterized by rigid-flexible coupling systems. The complex dynamic characteristics of mechanical structure of a stage, which are determined by structural and dynamic parameters, exert a serious influence on the accuracy of its motion and measurement. Systematic evaluation of such influence is essential for the design and improvement of stages. A systematic approach to modeling the dynamic accuracy of a nano-precision positioning stage is developed in this work by integrating a multi-rigid-body dynamic model of the mechanical system and measurement system models. The influence of structural and dynamic parameters, including aerostatic bearing configurations, motion plane errors, foundation vibrations, and positions of the acting points of driving forces, on dynamic accuracy is investigated by adopting the H-type configured stage as an example. The approach is programmed and integrated into a software framework that supports the dynamic design of nano-precision positioning stages. The software framework is then applied to the design of a nano-precision positioning stage used in a packaging lithography machine.

Keywords nano-precision positioning stage, analysis and design, structural and dynamic parameters, dynamic accuracy, systematic modeling

1 Introduction

Nano-precision positioning stages have been widely applied in semiconductor fabrication equipment, high-precision machine tools, and biomedical instruments to meet the requirements of large-range motion with high speed and extreme precision. The accuracy of nano-precision positioning stages has increased continually and reached the level of sub-nanometer in the past decades [1–3]. Emerging technologies, such as direct drive, floating support, flexible structures, and vibration isolation, have been utilized in nano-precision positioning stages to eliminate friction and reduce vibration transmission [2,4–7]. Thus, a nano-precision positioning stage is featured by a rigid-flexible coupling system, whose complex dynamic behavior is strongly determined by structural and dynamic parameters, such as mass properties of the moving parts, floating bearing configurations, form errors of motion planes, and foundation vibrations [7–9]. This complex dynamic behavior not only exerts a significant influence on motion accuracy but also varies the measurement beam paths of interferometers, which in turn affects measurement accuracy. A quantitative evaluation of the effects of these factors is crucial in designing mechanical systems of nano-precision positioning stages. However, understanding of the factors that affect dynamic errors, the extent of the effect, and the mechanisms behind the effect remains unknown. Therefore, a parameterized system accuracy model that considers multiple structural design factors and integrates dynamics and measurement is essential to achieve a comprehensive analysis of dynamic accuracy.

Many researchers have focused on addressing such issues and attempted to build system models for analyzing accuracy characteristics. The dynamic characteristics of ultra-precision motion systems and the influence of structural design factors on these dynamic characteristics have been investigated. For example, Chen et al. [10] and Li et al. [11] conducted a numerical analysis to investigate the influence of gas slip effects, gas supply pressure, and gap parameters on the bearing capacity characteristics of

Received January 31, 2019; accepted March 5, 2019

Chengyuan LIANG, Fang YUAN, Xuedong CHEN, Wei JIANG, Lizhan ZENG, Xin LUO (✉)

State Key Laboratory of Digital Manufacturing Equipment and Technology, Huazhong University of Science and Technology, Wuhan 430074, China
E-mail: mexinluo@hust.edu.cn

aerostatic bearings. He and Chen [12], Chen and Li [13], and Bao and Mao [14] established dynamic models of ultra-precision positioning stages, including equivalent models of aerostatic bearings, and analyzed the influence of the stiffness characteristics of aerostatic bearings on the dynamic behavior of the stages. Denkena et al. [15] established a finite element (FE) model of an ultra-precision positioning system and applied model order reduction to obtain a state space model for compensating dynamic errors. Li et al. [16] used an FE model to analyze and optimize the natural frequency of a micro grinding machine tool structure that contains a vertical motion stage. The H-type structural configuration is typical and popular in nano-precision positioning stages [2,17,18]. For the H-type stage, Chen et al. [19] proposed an assumed-mode method based on simplified mode shapes to formulate a dynamic model that considers beam flexibility. Kilikevičius and Kasparaitis [20] built an FE model of the H-type stage in an angle measurement comparator and investigated the influence of vibrations on carriage deformations, which increase the angle calibration error, by a modal analysis. However, these studies focused on specific instances of components and systems, and the analysis results are presented in the form of natural frequency, modal shapes, and transfer functions. Hence, they lack direct representations of motion and measurement result errors.

Researchers have also focused on the influence of structural design factors on the generation and propagation of motion and measurement errors. For example, for multi-axis precision machines, Zhou et al. [21], Guo et al. [22], Chen et al. [23], and Tian et al. [24] established mapping relationships between the main geometric errors on each axis and tool positioning accuracy and achieved system error compensations. Zhang et al. [25] and Cheng et al. [26] achieved optimal allocation of the geometric tolerances of each motion axis in multi-axis precision machines by analyzing the influence of geometric errors in the main structural parts on tool positioning errors. Liu et al. [27] established an error model of an H-type ultra-precision positioning stage that considers error factors, such as straightness, thermal deformation, structural deformation, and variations in air bearing gaps to evaluate measurement uncertainty. Gao et al. [28–30] analyzed the influence of the geometric and installation errors of interferometers and reflectors on measurement results by using a simplified model of the measurement beam path of interferometers; they designed a novel six-degree-of-freedom (6-DOF) measurement method for an ultra-precision motion platform and optimized the geometric tolerance allocation. Teng et al. [31] and Wen et al. [32] established an interferometer measurement model that considers the orientation errors of reflector mirrors to compensate the result errors of the measurement system of the ultra-precision motion platform. By analyzing laser ray paths affected by linear and angular errors of interferometers and optics, Liu et al. [33] developed a 6-DOF geometric error measurement method for a long linear stage.

However, most of the error analyses in these studies either considered only the static error factors in structures, or simplified dynamic error factors into static error factors. These analyses lacked the evaluations of the influences of static error factors on the dynamic behavior of the mechanical systems and the resulting dynamic errors in motion and measurement.

It is essential to model and simulate a large number of system instances with various design factor configurations to comprehensively analyze the influence of structural and dynamic design factors on system dynamic errors. Therefore, a systematic accuracy modeling method should be parameterized and modularized. Modifying parameter values and replacing modules can rapidly modify design factors, such as aerostatic bearing configurations, mass properties of main structural parts, flatness errors of motion planes, external excitations, and even the configurations of measurement and mechanical systems. In the above-mentioned studies, accurate models were built for specific and detailed instances of systems and components. However, these models are complex. Integrating them into a systematic accuracy model, modifying their design factors, and changing their system configurations are difficult.

A parameterized dynamic accuracy model of the H-type nano-precision positioning stage is built in the current study, and the effects of structural design factors on the dynamic errors are analyzed comprehensively. The system dynamic accuracy model integrates the multi-rigid-body dynamic model of the mechanical system and the measurement models. Nonlinear stiffness models of aerostatic bearings are built in the dynamic model, which consider the influence of the flatness errors of motion planes. Homogeneous transformation matrices, which represent the pose of the plane mirrors with respect to the interferometers, are used as interfaces to connect the dynamic model and measurement models. The effects of the positions of acting points of the driving and aerostatic bearing supporting forces, the nonlinear stiffness of aerostatic bearings, the motion plane errors, and the foundation vibrations on the dynamic errors are analyzed based on the system dynamic accuracy model. The systematic modeling and analysis approaches are programmed as the parameterized model templates of key modules in the system dynamic accuracy model and the simulation scripts for dynamic error analysis. The model templates and simulation scripts are integrated into the prototype system of a software framework supporting the dynamic design of nano-precision positioning stages.

The remaining parts of this work are organized as follows. The modeling approach for the dynamic accuracy of the H-type stage is introduced in Section 2. The influence of structural and dynamic design factors on dynamic errors is analyzed in Section 3. In Section 4, the

modeling and analysis approach is programmed and integrated into a software framework supporting the dynamic design of nano-precision positioning stages. The conclusions are drawn in Section 5.

2 Dynamic accuracy modeling of H-type nano-precision positioning stage

2.1 Structural and measurement configurations of an H-type nano-precision positioning stage

An H-type nano-precision positioning stage is investigated, which adopts a single stage configuration to achieve nano-precision motion in *x*, *y*, and *Rz* directions. The movement range of the H-type stage is 200 mm. The measurement resolution of the interferometer system is 0.15 nm. Within 0.5 s after completing a stepping motion, the mean of the positioning error is less than 20 nm, and the maximum standard deviation is less than 35 nm.

As shown in Fig. 1, the H-type stage consists of a base, a beam, and a slider. The beam is driven by two *x*-direction linear motors, and the beam can move in the *x* direction and rotate in a small range in the *Rz* direction. The slider is driven by a *y*-direction linear motor and can translate on the beam in the *y* direction. A micro-motion stage is usually attached to the slider to achieve nano-precision movement in a small range.

A 3-DOF measurement system based on interferometers is built in the H-type stage. The measurement system uses a $2+1$ layout that includes a one-axis interferometer in the *x* direction and a two-axis interferometer in the *y* direction [29]. The interferometers are fixed on the base, and the long plane mirrors are mounted on the slider. The translational displacements along *x* and *y* directions and the rotational displacement around the *z* axis can be measured. Hence, *x*, *y*, and *Rz* are defined as controlled directions, and *z*, *Rx*, and *Ry* are defined as non-controlled directions.

The base is supported by vibration isolators to isolate vibrations transferred from the foundation. The beam is supported on the base by AB_bb_v1 and AB_bb_v2. Each group consists of two aerostatic bearings arranged along the *x* direction and is preloaded by permanent magnets [2]. AB_bb_h is attached to the beam with flexure hinges and adsorbed on the *x* guide mounted on the base. AB_bb_h consists of six bearings and is also preloaded by permanent magnets. The slider is supported on the base by AB_bs_v, which consists of four bearings and is preloaded by air vacuum [2]. AB_bs_h is mounted on the slider and adsorbed on the *y* guide on both sides of the beam. AB_bs_h consists of four bearings and is preloaded by an opposite bearing arrangement [2].

2.2 Dynamic modeling of the H-type stage

The dynamic topology of the H-type stage is shown in Fig. 2. It includes three rigid bodies, namely, base, beam, and slider. The base is affected by foundation vibrations. O_w is defined as the global reference frame. Body-fixed

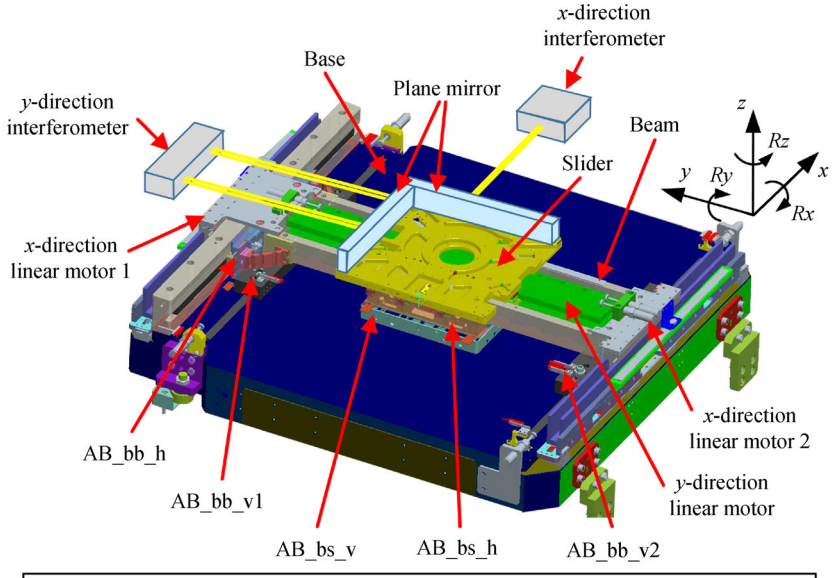

Fig. 1 Structure of the H-type nano-precision positioning stage

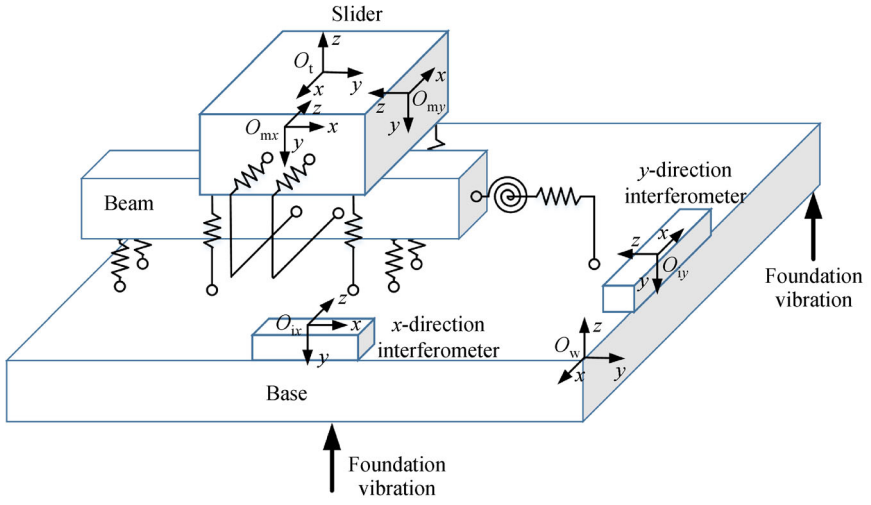

Fig. 2 Dynamic topology of the H-type nano-precision positioning stage

frames O_{bs}, O_{bm}, and O_{sc} are placed at the mass centers of the base, beam, and slider, respectively. Body-fixed frame O_t is placed on the slider to represent the pose (position and orientation) of the operating point during system motion. Body-fixed frames O_{ix} and O_{iy} are fixed on the base and represent the poses of the x- and y-direction interferometers, respectively. Body-fixed frames O_{mx} and O_{my} are placed on the slider and represent the poses of the x- and y-direction plane reflector mirrors, respectively.

The aerostatic bearing group can be modeled as a combination of distributed single bearing models. As shown in Fig. 3, a single aerostatic bearing can be equivalently modeled as a spring with nonlinear stiffness [14,34]. In the aerostatic bearing model, one acting point is fixed on the moving part and defined as F_{ab}. The other acting point is defined as B'_{ab} and can slide on the supporting surface as the moving part moves. The flatness error of the supporting surface is considered. e_z is the normal distance between B'_{ab} and its projection B_{ab} on the ideal supporting surface. The normal direction of the supporting surface changes minimally during system motion. Hence, we can assume that the direction of the supporting force is always perpendicular to the ideal supporting surface.

If the supply gas pressure is stable, then the relationship between steady supporting force F_{Kab} and gas film thickness h in an aerostatic bearing model can be fitted by Richards model. The steady supporting force can be presented as

$$F_{Kab} = \frac{a}{\left(1+e^{(b-ch)}\right)^{\frac{1}{d}}} = \frac{a}{\left(1+e^{(b-c(z_F-z_B-e_z))}\right)^{\frac{1}{d}}}, \quad (1)$$

where z_F and z_B are the z-direction coordinates of F_{ab} and B_{ab}, and a, b, c, and d are the coefficients of Richards model and can be obtained by fitting the experimental or simulation results of aerostatic bearing capacity. As shown in Fig. 4, the accuracy of Richards model can be verified by citing experimental data from Ref. [35].

The displacements of the base, beam, and slider can be

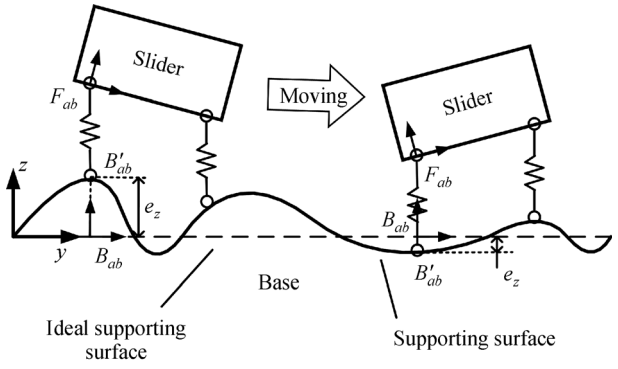

Fig. 3 Equivalent dynamic model of a single aerostatic bearing

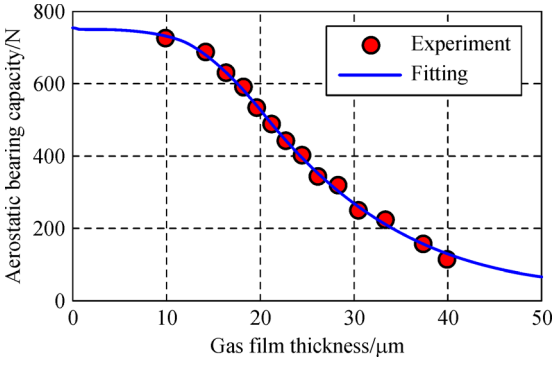

Fig. 4 Experimental data of aerostatic bearing capacity [35] and fitting curve based on Richards model

represented by the generalized coordinates $\boldsymbol{q}_{\mathrm{bs}}$, $\boldsymbol{q}_{\mathrm{bm}}$, and $\boldsymbol{q}_{\mathrm{sc}}$, respectively. The dynamic model of the H-type stage can be expressed in the matrix form:

$$\boldsymbol{M}\frac{\mathrm{d}^2\boldsymbol{q}}{\mathrm{d}t^2}+\boldsymbol{C}\frac{\mathrm{d}\boldsymbol{q}}{\mathrm{d}t}+\boldsymbol{K}\boldsymbol{q}=\boldsymbol{F}, \tag{2}$$

where $\boldsymbol{q}=[\boldsymbol{q}_{\mathrm{bs}};\boldsymbol{q}_{\mathrm{bm}};\boldsymbol{q}_{\mathrm{sc}}]$, t is the time, $\boldsymbol{M}$ is the generalized mass matrix, $\boldsymbol{C}$ is the damping matrix, $\boldsymbol{K}$ is the stiffness matrix, and $\boldsymbol{F}$ is the external excitation that includes driving forces and foundation vibrations.

The parameterized system dynamic model has been verified to be correct by establishing a dynamic model based on the parameterized model for an instance of H-type nano-precision positioning stage and by comparing its mode results with the FEM reference results, which have been verified through experiments.

2.3 Measurement model of an interferometer

The ideal measurement beam path of a single-axis plane mirror interferometer is presented in Fig. 5(a) [36]. The plane mirror reflector and the interferometer have the same orientation. R is the mirror image of the cube corner R' relative to the polarizing beam splitter. Hence, the beam path lengths have the following relation: $|PC'|=|PC|$, $|D'Q|=|DQ|$. The beam transmitted from the interferometer is reflected back by the plane mirror. After being reflected by the beam splitter and cube corner, it is transmitted to the plane mirror again and reflected back to the receiver finally. The beam path lengths have the following relation: $|AB|=|BC|=|DE|=|EF|$.

The actual measurement beam path is presented in Fig. 5(b). The plane mirror is deflected relative to the interferometer. Thus, the measurement beam is not perpendicular to the mirror. The measurement beam is returned to the receiver through the path $A\rightarrow B\rightarrow P\rightarrow C'\rightarrow D'\rightarrow Q\rightarrow E\rightarrow F$.

Body-fixed frame O_{M_xyz} is placed at the center of the plane mirror surface, whose z-axis is perpendicular to the mirror surface. Body-fixed frame O_{I_xyz} is defined on the output aperture of the interferometer. Its z-axis is perpendicular to the aperture surface, parallel to the exit beam, and coincides with the central axis of R. Body-fixed frame O_{A_xyz} is placed at the exit Point A of the measurement beam path. Its orientation is consistent with that of O_{I_xyz}.

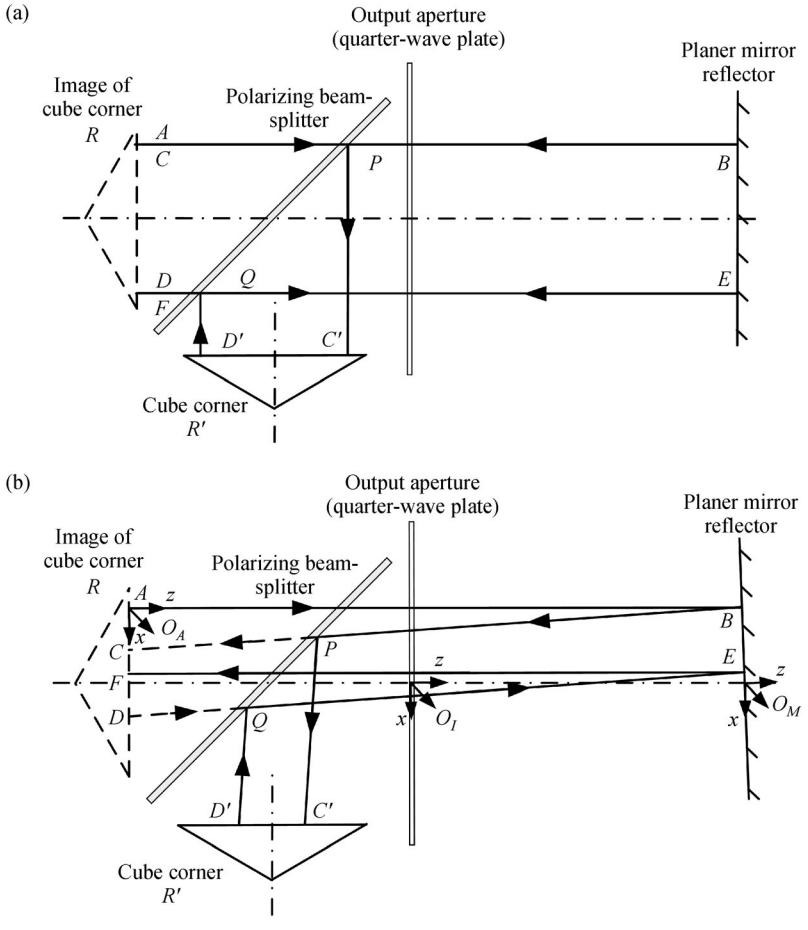

Fig. 5 Measurement beam path of a single-axis plane mirror interferometer. (a) Ideal beam path; (b) actual beam path

The pose of coordinate frame O_j with respect to another coordinate frame O_i can be represented as homogeneous transformation matrix ${}^{i}_{j}\boldsymbol{T}$. In frame O_{i_xyz}, a point can be represented as $\boldsymbol{P}^i = (x^i, y^i, z^i, 1)^{\mathrm{T}}$, and a vector can be represented as $\boldsymbol{V}^i = (x^i, y^i, z^i, 0)^{\mathrm{T}}$.

If the distance between the output aperture and R is L_n and the distances between exit Point A and the central axis of R are x_A^I and y_A^I, then the homogeneous transformation matrix from O_{M_xyz} to O_{A_xyz} is

$$ {}^{A}_{M}\boldsymbol{T} = ({}^{I}_{A}\boldsymbol{T})^{-1} \cdot {}^{I}_{M}\boldsymbol{T} = \begin{bmatrix} 1 & 0 & 0 & x_A^I \\ 0 & 1 & 0 & y_A^I \\ 0 & 0 & 1 & -L_n \\ 0 & 0 & 0 & 1 \end{bmatrix}^{-1} \cdot {}^{I}_{M}\boldsymbol{T}. \quad (3) $$

In the frame O_{A_xyz}, the coordinates of Point A are $\boldsymbol{P}_A^A = (0,0,0,1)^{\mathrm{T}}$. The coordinates of the origin M of the frame O_{M_xyz} are $\boldsymbol{P}_M^A = {}^{A}_{M}\boldsymbol{T} \cdot \boldsymbol{P}_M^M = {}^{A}_{M}\boldsymbol{T} \cdot (0,0,0,1)^{\mathrm{T}}$. The normal vector of the plane mirror surface is $\boldsymbol{V}_{Mn}^A = {}^{A}_{M}\boldsymbol{T} \cdot \boldsymbol{V}_{Mn}^M = {}^{A}_{M}\boldsymbol{T} \cdot (0,0,-1,0)^{\mathrm{T}}$.

The equation of plane mirror surface S_M^A is

$$ \boldsymbol{V}_{Mn}^{A\prime} \cdot (\boldsymbol{P}^A - \boldsymbol{P}_M^A) = 0. \quad (4) $$

Point B is the intersection of S_M^A and the planes $(x^A = 0)$ and $(y^A = 0)$. Hence, its coordinates in the frame O_{A_xyz} are

$$ \boldsymbol{P}_B^A = \begin{bmatrix} \boldsymbol{V}_{Mn}^{A\prime} \\ 0 & 1 & 0 & 0 \\ 1 & 0 & 0 & 0 \\ 0 & 0 & 0 & 1 \end{bmatrix}^{-1} \begin{bmatrix} \boldsymbol{V}_{Mn}^{A\prime} \cdot \boldsymbol{P}_M^A \\ 0 \\ 0 \\ 1 \end{bmatrix}. \quad (5) $$

If $\boldsymbol{L}_{Bn}$ is the normal vector of the plane mirror surface and passes Point B, then Point $A1$, which is the symmetric point of Point A with respect to $\boldsymbol{L}_{Bn}$, is on the reflected beam path BC. The coordinates of Point $A1$ are

$$ \boldsymbol{P}_{A1}^A = 2\boldsymbol{P}_B^A - 2\frac{\boldsymbol{V}_{Mn}^{A\prime} \cdot \boldsymbol{P}_B^A}{\boldsymbol{V}_{Mn}^{A\prime} \cdot \boldsymbol{V}_{Mn}^A} \cdot \boldsymbol{V}_{Mn}^A - \boldsymbol{P}_A^A. \quad (6) $$

Point C is the intersection of R and beam path BC, and its coordinates are

$$ \boldsymbol{P}_C^A = -\frac{(0,0,1,0)\boldsymbol{P}_B^A}{(0,0,1,0)(\boldsymbol{P}_{A1}^A - \boldsymbol{P}_B^A)} \cdot (\boldsymbol{P}_{A1}^A - \boldsymbol{P}_B^A) + \boldsymbol{P}_B^A. \quad (7) $$

According to the characteristic of the cube corner, exit Point D and incident Point C are symmetrical with respect to the central axis of R. Incident beam BC is in the same direction as exit beam DE. Hence, the coordinates of Points D, E, and F are

$$ \boldsymbol{P}_D^A = ({}^{I}_{A}\boldsymbol{T})^{-1} \cdot \begin{bmatrix} -1 & 0 & 0 & 0 \\ 0 & -1 & 0 & 0 \\ 0 & 0 & 1 & 0 \\ 0 & 0 & 0 & 1 \end{bmatrix} \cdot ({}^{I}_{A}\boldsymbol{T} \cdot \boldsymbol{P}_C^A), \quad (8) $$

$$ \boldsymbol{P}_E^A = \frac{\boldsymbol{V}_{Mn}^{A\prime} \cdot (\boldsymbol{P}_M^A - \boldsymbol{P}_D^A)}{\boldsymbol{V}_{Mn}^{A\prime} \cdot (\boldsymbol{P}_B^A - \boldsymbol{P}_C^A)} \cdot (\boldsymbol{P}_B^A - \boldsymbol{P}_C^A) + \boldsymbol{P}_D^A, \quad (9) $$

$$ \boldsymbol{P}_F^A = \begin{bmatrix} 1 & 0 & 0 & 0 \\ 0 & 1 & 0 & 0 \\ 0 & 0 & 0 & 0 \\ 0 & 0 & 0 & 1 \end{bmatrix} \cdot \boldsymbol{P}_E^A. \quad (10) $$

The lengths of the beam paths, $|AB|$, $|BC|$, $|DE|$, and $|EF|$, can be obtained according to the coordinates of Points A, B, C, D, E, and F. If the beam path in the cube corner is ignored, then the total length of the measurement beam path is

$$ L = |AB| + |BC| + |DE| + |EF|. \quad (11) $$

The total length of the measurement beam path at the initial time is L_0, and it becomes L_t at a certain moment t. The interferometer's reading is

$$ ML_t = (L_t - L_0)/4. \quad (12) $$

In the measurement model of the single-axis plane mirror interferometer, all parameters, except ${}^{I}_{M}\boldsymbol{T}$, are constant structural parameters of the interferometer. Thus, the measurement model can be packaged as a function $f_{\mathrm{m}}()$ with ${}^{I}_{M}\boldsymbol{T}$ as the input parameter and can be expressed as

$$ \boldsymbol{ML} = f_{\mathrm{m}}({}^{I}_{M}\boldsymbol{T}). \quad (13) $$

2.4 Structure-motion-measurement integrated modeling for system accuracy analysis

Generalized coordinates $\boldsymbol{q}_{\mathrm{bs}}$, $\boldsymbol{q}_{\mathrm{bm}}$, and $\boldsymbol{q}_{\mathrm{sc}}$ can be calculated by solving the dynamic model of the H-type stage. Homogeneous transformation matrix ${}^{\mathrm{w}}_{\mathrm{i}}\boldsymbol{T}$ can be established (i = bs, bm, sc) based on $\boldsymbol{q}_{\mathrm{bs}}$, $\boldsymbol{q}_{\mathrm{bm}}$, and $\boldsymbol{q}_{\mathrm{sc}}$. Constant homogeneous transformation matrix ${}^{\mathrm{sc}}_{\mathrm{t}}\boldsymbol{T}$ can also be established according to the structural features of the slider. Hence, during motion simulation, homogeneous transformation matrix ${}^{\mathrm{w}}_{\mathrm{t}}\boldsymbol{T}$ can be calculated in real time based on ${}^{\mathrm{w}}_{\mathrm{sc}}\boldsymbol{T}$ and ${}^{\mathrm{sc}}_{\mathrm{t}}\boldsymbol{T}$. Given that the rotation angle of the slider is small during system motion, the displacements of the operating point with respect to O_{w} can be obtained from the matrix element of ${}^{\mathrm{w}}_{\mathrm{t}}\boldsymbol{T}$.

$$ {}^{\mathrm{w}}_{\mathrm{t}}\boldsymbol{T} = {}^{\mathrm{w}}_{\mathrm{sc}}\boldsymbol{T} \cdot {}^{\mathrm{sc}}_{\mathrm{t}}\boldsymbol{T} \approx \begin{bmatrix} 1 & -\theta^{\mathrm{w}}_{zt} & \theta^{\mathrm{w}}_{yt} & x^{\mathrm{w}}_{\mathrm{t}} \\ \theta^{\mathrm{w}}_{zt} & 1 & -\theta^{\mathrm{w}}_{xt} & y^{\mathrm{w}}_{\mathrm{t}} \\ -\theta^{\mathrm{w}}_{yt} & \theta^{\mathrm{w}}_{xt} & 1 & z^{\mathrm{w}}_{\mathrm{t}} \\ 0 & 0 & 0 & 1 \end{bmatrix}. \quad (14) $$

The homogeneous transformation matrices of the interferometers and plane reflector mirrors relative to O_{w} can also be calculated by

$$ \begin{cases} {}^{\mathrm{w}}_{\mathrm{m}x}\boldsymbol{T} = {}^{\mathrm{w}}_{\mathrm{sc}}\boldsymbol{T}\,{}^{\mathrm{sc}}_{\mathrm{m}x}\boldsymbol{T}, \\ {}^{\mathrm{w}}_{\mathrm{i}x}\boldsymbol{T} = {}^{\mathrm{w}}_{\mathrm{bs}}\boldsymbol{T}\,{}^{\mathrm{bs}}_{\mathrm{i}x}\boldsymbol{T}, \\ {}^{\mathrm{w}}_{\mathrm{m}y}\boldsymbol{T} = {}^{\mathrm{w}}_{\mathrm{sc}}\boldsymbol{T}\,{}^{\mathrm{sc}}_{\mathrm{m}y}\boldsymbol{T}, \\ {}^{\mathrm{w}}_{\mathrm{i}y}\boldsymbol{T} = {}^{\mathrm{w}}_{\mathrm{bs}}\boldsymbol{T}\,{}^{\mathrm{bs}}_{\mathrm{i}y}\boldsymbol{T}, \end{cases} \quad (15) $$

where ${}^{\mathrm{bs}}_{\mathrm{i}x}\boldsymbol{T}$ and ${}^{\mathrm{bs}}_{\mathrm{i}y}\boldsymbol{T}$ represent the installation poses of the x- and y-direction interferometers relative to O_{bs} and ${}^{\mathrm{sc}}_{\mathrm{m}x}\boldsymbol{T}$ and ${}^{\mathrm{sc}}_{\mathrm{m}y}\boldsymbol{T}$ represent the installation poses of the x- and y-direction plane mirrors relative to O_{sc}. These matrices are all constant and can be established according to the structural features of the H-type stage.

Multi-axis plane mirror interferometers are often used in nano-precision positioning stages [28–32,36]. The measurement model of a multi-axis interferometer can be composed of multiple models of single-axis interferometers. The ${}^{ii}_{\mathrm{m}i}\boldsymbol{T}$ required for each single-axis interferometer model can be converted from ${}^{\mathrm{w}}_{\mathrm{i}}\boldsymbol{T}$ and ${}^{\mathrm{w}}_{\mathrm{m}}\boldsymbol{T}$, which represent the overall poses of the interferometer and plane mirror. Given that the matrices representing the overall poses of the interferometers and plane mirrors can be obtained from the dynamic model by Eq. (15), interferometer models can be connected to the dynamic model with matrices ${}^{\mathrm{w}}_{\mathrm{i}x}\boldsymbol{T}$, ${}^{\mathrm{w}}_{\mathrm{i}y}\boldsymbol{T}$, ${}^{\mathrm{w}}_{\mathrm{m}x}\boldsymbol{T}$, and ${}^{\mathrm{w}}_{\mathrm{m}y}\boldsymbol{T}$ as interfaces. The interferometer readings in the measurement system can be obtained by

$$ \begin{cases} X = f_{\mathrm{m}}({}^{\mathrm{ix}}_{\mathrm{m}x}\boldsymbol{T}) = f_{\mathrm{m}}(({}^{\mathrm{w}}_{\mathrm{i}x}\boldsymbol{T})^{-1}\,{}^{\mathrm{w}}_{\mathrm{m}x}\boldsymbol{T}), \\ Y_1 = f_{\mathrm{m}}({}^{\mathrm{iy1}}_{\mathrm{m}y1}\boldsymbol{T}) = f_{\mathrm{m}}(({}^{\mathrm{w}}_{\mathrm{i}y1}\boldsymbol{T})^{-1}\,{}^{\mathrm{w}}_{\mathrm{m}y1}\boldsymbol{T}) \\ \quad = f_{\mathrm{m}}(({}^{\mathrm{w}}_{\mathrm{i}y}\boldsymbol{T}\,{}^{\mathrm{iy}}_{\mathrm{i}y1}\boldsymbol{T})^{-1}({}^{\mathrm{w}}_{\mathrm{m}y}\boldsymbol{T}\,{}^{\mathrm{my}}_{\mathrm{m}y1}\boldsymbol{T})), \\ Y_2 = f_{\mathrm{m}}({}^{\mathrm{iy2}}_{\mathrm{m}y2}\boldsymbol{T}) = f_{m}(({}^{\mathrm{w}}_{\mathrm{i}y2}\boldsymbol{T})^{-1}\,{}^{\mathrm{w}}_{\mathrm{m}y2}\boldsymbol{T}) \\ \quad = f_{\mathrm{m}}(({}^{\mathrm{w}}_{\mathrm{i}y}\boldsymbol{T}\,{}^{\mathrm{iy}}_{\mathrm{i}y2}\boldsymbol{T})^{-1}({}^{\mathrm{w}}_{\mathrm{m}y}\boldsymbol{T}\,{}^{\mathrm{my}}_{\mathrm{m}y2}\boldsymbol{T})). \end{cases} \quad (16) $$

The reading outputs from the interferometers models are converted into the displacement measurement results of the operating point by a displacement solving algorithm corresponding to the layout of interferometers [29,37]. If D_{b} is the distance between the two y-direction measurement beam axes, then displacement measurement results x, y, and θ_z are calculated as

$$ \begin{bmatrix} x \\ y \\ \theta_z \end{bmatrix} = \begin{bmatrix} 1 & 0 & 0 \\ 0 & \frac{1}{2} & \frac{1}{2} \\ 0 & \frac{1}{D_{\mathrm{b}}} & \frac{-1}{D_{\mathrm{b}}} \end{bmatrix} \begin{bmatrix} X \\ Y_1 \\ Y_2 \end{bmatrix}. \quad (17) $$

The system dynamic model and the interferometer measurement models can be integrated using Eqs. (15) and (16). After combining with Eqs. (14) and (17) and other modules, a system dynamic accuracy model can be created to analyze the motion errors and the errors of displacement measurement results during system motion, as shown in Fig. 6. The signals of ideal displacements and ideal accelerations are outputted from the movement trajectory generator. The ideal acceleration signals are converted into the driving forces of the linear motors by the driving force assignment module and applied to the system dynamic model. During system motion simulation, the displacements of the operating point are outputted from the system dynamic model in real time together with the values of ${}^{\mathrm{w}}_{\mathrm{i}x}\boldsymbol{T}$, ${}^{\mathrm{w}}_{\mathrm{i}y}\boldsymbol{T}$, ${}^{\mathrm{w}}_{\mathrm{m}x}\boldsymbol{T}$, and ${}^{\mathrm{w}}_{\mathrm{m}y}\boldsymbol{T}$. System motion errors are calculated based on the outputted displacements. The values of ${}^{\mathrm{w}}_{\mathrm{i}x}\boldsymbol{T}$, ${}^{\mathrm{w}}_{\mathrm{i}y}\boldsymbol{T}$, ${}^{\mathrm{w}}_{\mathrm{m}x}\boldsymbol{T}$, and ${}^{\mathrm{w}}_{\mathrm{m}y}\boldsymbol{T}$ are received by the interferometer measurement models and used to calculate the displacement measurement result errors.

Random foundation vibration excitations are outputted from the foundation vibration generator and applied to the system dynamic model. The flatness error generator receives the current coordinates of each aerostatic bearing model and returns the flatness error value e_{zi} required for calculating the supporting force of the aerostatic bearing model. To emphasize the characteristics of the mechanical system, the system dynamic accuracy model is open-loop and does not include feedback control.

3 Quantitative analysis of the influence of structural design factors

The important structural design factors of nano-precision positioning stages include the positional deviations of the driving force acting points and center points of aerostatic bearing groups with respect to the mass centers of main structural parts, the stiffness characteristics of aerostatic bearings, the flatness tolerances of motion planes, and the foundation vibration characteristics. These design factors affect the system dynamic characteristics and are the main design goals and constraints in main structure design, aerostatic bearing selection, motion plane machining, and vibration isolation system design. In this section, the influences of these design factors on system motion and measurement result errors are analyzed using the system dynamic accuracy model.

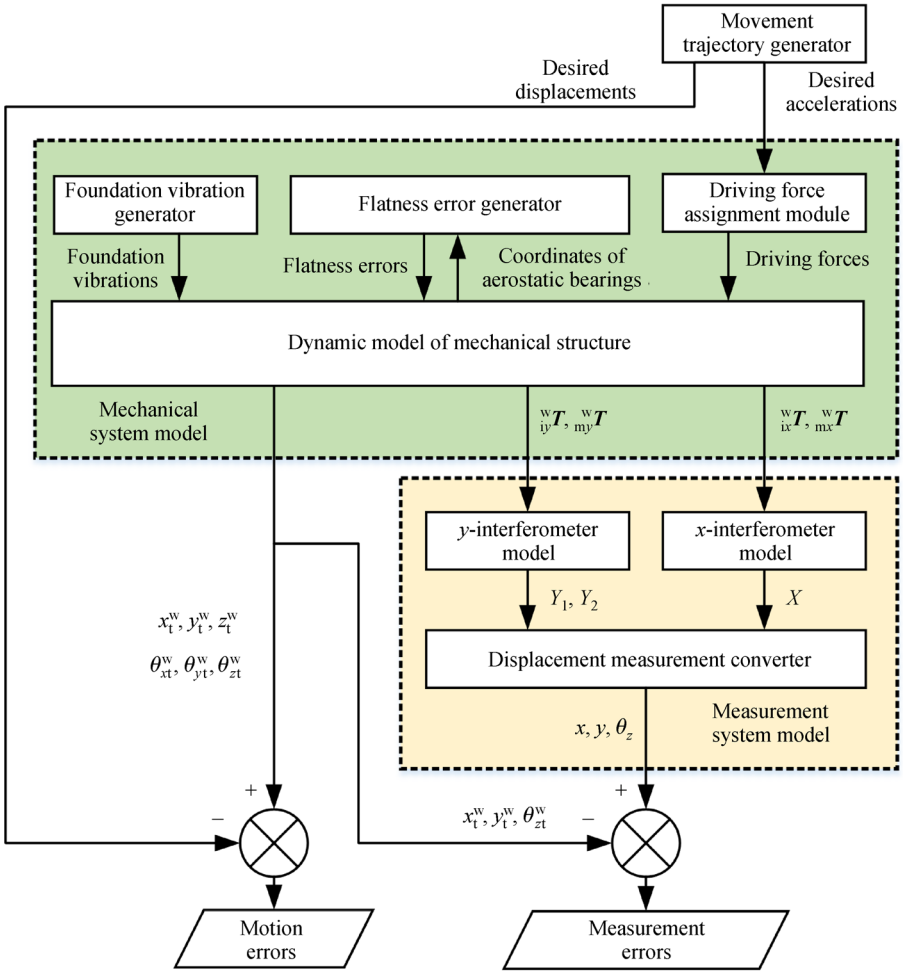

Fig. 6 System dynamic accuracy model

3.1 Influence of locations of driving force acting points

3.1.1 Simulation setup

In this section, Δz_{Fx} is defined to represent the z-direction displacements of the acting points of the x-direction driving forces with respect to the mass center of the x-direction moving part (beam + slider). Similarly, the displacements of the acting point of the y-direction driving force relative to the mass center of the slider are defined as Δx_{Fy} and Δz_{Fy}. By setting the position parameters of the acting points of driving forces in the parameterized system dynamic accuracy model, the values of Δz_{Fx}, Δx_{Fy}, and Δz_{Fy} are changed, and their influences on the motion errors and measurement result errors are simulated and analyzed.

During motion simulation, the operating point completes a "scan–step–scan" movement, and its trajectory is shown in Fig. 7. During scanning, the maximum acceleration ($a_{\max}$) is 9.81 m/s^2, and the scanning speed (v) is 250 mm/s. During stepping, the maximum acceleration is 6.03 m/s^2, and the maximum stepping speed is 400 mm/s. The trajectory is employed, and the errors in different phases of the motion are investigated in the subsequent simulations.

3.1.2 Results and discussion

As shown in Fig. 8, the positioning errors of the original model increase constantly in x and y directions because the driving force assignment module in the system dynamic accuracy model is designed based on the assumption that the joints in the mechanical system are ideal. In the driving force assignment module, the effect of the flexibleness of the aerostatic bearings and flexible hinges is disregarded, thus causing driving errors. Hence, the beam and slider fail to stop accurately at the end of the scanning and stepping movements.

The driving force in the x direction is transferred to the slider through the aerostatic bearing group AB_bs_h. The position of AB_bs_h is not subject to Δz_{Fx}. Hence, Δz_{Fx} has little inference on the dynamic errors during the accelerating and decelerating phases in the scanning

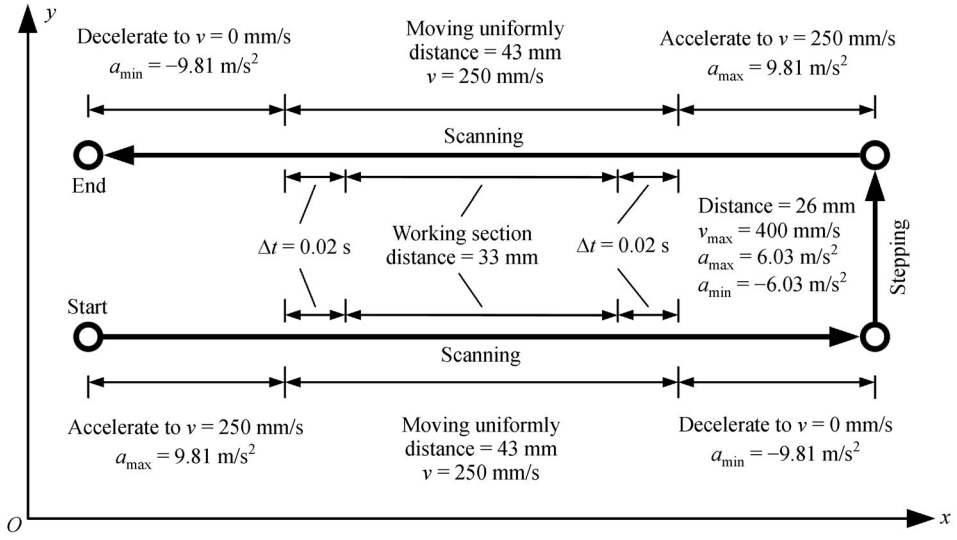

Fig. 7 Movement trajectory in system simulation

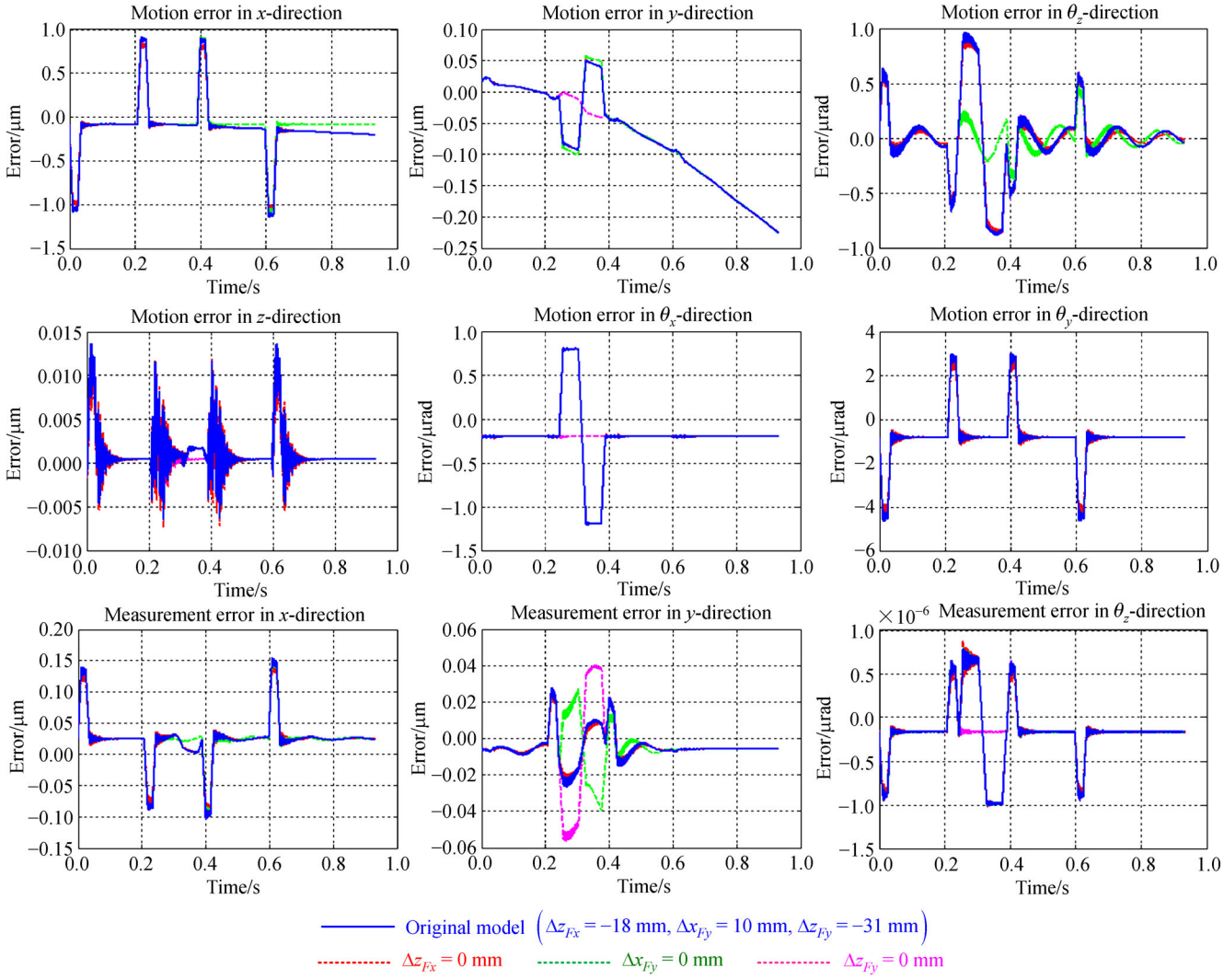

Fig. 8 Simulation results of dynamic errors corresponding to different positions of driving force acting points

movements. However, Δz_{Fx} affects the pose oscillation of the beam during the working phases in the scanning movements, consequently affecting the vibrations of the slider through AB_bs_h. The slider is directly driven by the *y*-direction driving force. Thus, Δx_{Fy} and Δz_{Fy} have a significant influence on the dynamic errors during the stepping movement.

The detailed analysis results of the effects on dynamic errors are given in Table 1, which includes the motion errors in controlled directions e_x, e_y, and $e_{\theta z}$, the motion errors in non-controlled directions e_z, $e_{\theta x}$, and $e_{\theta y}$, and the measurement result errors $e_{\mathrm{m}x}$, $e_{\mathrm{m}y}$, and $e_{\mathrm{m}\theta z}$. In Table 1, Sca signifies the error in the accelerating and decelerating phases of the scanning motion; and Scw signifies the error in the working phases of the scanning motion; St signifies the error in the stepping motion; and PE signifies the positioning error after the scanning and stepping motion.

The motion errors in *Rx* and *Rz* directions affect the measurement result errors in *y* direction, as shown in Fig. 8, because the rotations of the slider in *Rx* and *Rz* directions change the incident angle of the *y*-direction measurement beam on the planar mirror. Hence, the length of the measurement beam path and the displacement measurement result in *y* direction are changed. Similarly, the measurement result error in *x* direction is affected by the motion errors in *Ry* and *Rz* directions.

3.2 Influence of aerostatic bearing group configurations

3.2.1 Simulation setup

In this section, the relationship between system dynamic errors and the positions of the center points of aerostatic bearing groups is discussed. The center point of the combination of AB_bb_v1 and AB_bb_v2 is defined as P_{bbv}, and the center points of AB_bb_h, AB_bs_v, and AB_bs_h are defined as P_{bbh}, P_{bsv}, and P_{bsh}, respectively. The *x*- and *y*-direction displacements of P_{bbv} relative to the mass center of the beam are defined as Δx_{bbv} and Δy_{bbv}, respectively. Δx_{bbh} and Δz_{bbh} represent the displacements of P_{bbh} in *x* and *z* directions with respect to the mass center of the beam. Similarly, Δx_{bsv} and Δy_{bsv} represent the *x*- and *y*-direction displacements of P_{bsv} relative to the mass center of the slider, and the displacements of P_{bsh} relative to the mass center of the slider are defined as Δx_{bsh}, Δy_{bsh}, and Δz_{bsh}. By modifying the layout of each aerostatic bearing group in the parameterized dynamic accuracy model, different sets of values are assigned to the displacements, and corresponding system errors are simulated and analyzed.

Next, the effects of aerostatic bearing stiffness on system dynamic errors are discussed. K_{bbv} is defined to represent the stiffness of the bearings used in AB_bb_v1 and AB_bb_v2; K_{bbh}, K_{bsv}, and K_{bsh} represent the stiffness of the bearings in AB_bb_h, AB_bs_v, and AB_bs_h, respectively. By setting the values of K_{bbv}, K_{bbh}, K_{bsv}, and K_{bsh} in the parameterized system dynamic accuracy model, the effects of the stiffness of each aerostatic bearing group on dynamic errors are simulated and analyzed.

The influence of the nonlinear stiffness characteristics of aerostatic bearing on system dynamic errors is also discussed.

The effects of two kinds of equivalent aerostatic bearing models on system dynamic errors are compared. In one model, the stiffness value of aerostatic bearing is constant. The other model is the equivalent dynamic model with nonlinear stiffness and is based on Richards model. Two system models using the aerostatic bearing models are built. By setting the preloading parameter values, the rated operating stiffness values of the nonlinear models in one system model are consistent with the stiffness values of the corresponding constant models in the other system model. The two system models are simulated under conditions of no preloading error, errors in the preloading force of magnetic and vacuum preloading, and errors in the initial gas film thickness of the opposite bearing arrangement.

The effects of different nonlinear stiffness models with the same rated operating stiffness are also compared, as shown in Fig. 9. Models 1 and 2 use the same type of aerostatic bearing, but the supply pressures are different. Model 3 uses another type of aerostatic bearing. The rated operating stiffness of Model 1 is close to its maximum stiffness.

3.2.2 Results and discussion

Δx_{bbv}, Δy_{bbv}, Δx_{bbh}, Δz_{bbh}, and Δx_{bsh} do not have a substantial effect on system dynamic errors. As shown in Figs. 10–12, Δx_{bsv} and Δy_{bsv} mainly affect static balance errors and static measurement result errors, and Δy_{bsh} and Δz_{bsh} affect dynamic errors in the acceleration and

Table 1 Effects of the positions of driving force acting points on dynamic errors

Displacement of the driving force acting point	e_x	e_y	$e_{\theta z}$	e_z	$e_{\theta x}$	$e_{\theta y}$	$e_{\mathrm{m}x}$	$e_{\mathrm{m}y}$	$e_{\mathrm{m}\theta z}$
Δz_{Fx} ↓	Sca ↑, Scw ↓, St ↑	Scw ↓	Sca ↑, Scw ↓, St ↑	Scw ↓	Scw ↓	Sca ↑, Scw ↓, St ↑	Sca ↑, Scw ↓, St ↑	Sca ↑, St ↑	Sca ↑, Scw ↓, St ↑
$\lvert\Delta x_{Fy}\rvert$ ↓	PE ↓	(Δx_{Fy}↓) St ↑	St ↓				St ↓	(Δx_{Fy}↓) St ↑	
$\lvert\Delta z_{Fy}\rvert$ ↓		St ↓		St ↓	St ↓			(Δz_{Fy}↓) St ↓	St ↓

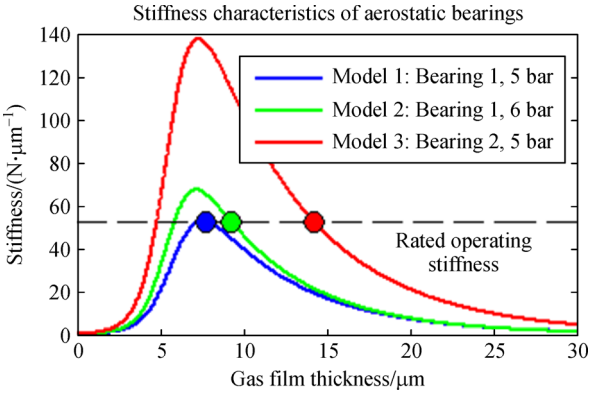

Fig. 9 Aerostatic bearing models with different stiffness characteristics. 1 bar = 10^5 Pa

deceleration phases of scanning movements. $\Delta y_{bsh} \neq 0$ is one of the main reasons for the increasing positioning error in y direction. Detailed analysis results on the effects on dynamic errors are given in Table 2.

K_{bbv} and K_{bbh} have minimal influence on dynamic accuracy. Increasing K_{bsv} and K_{bsh} reduces not only the errors in the stepping motion and the acceleration and deceleration phases of the scanning motions, but also the vibrations during the working phases in the scanning motions, as shown in Table 3. AL signifies the error of the entire process; SS signifies the error in the entire scanning and stepping motions; and SB signifies the static balance error.

Figure 13 shows the comparison results of the dynamic errors corresponding to the constant stiffness and nonlinear stiffness models. During the stepping motion and acceleration and deceleration phases of scanning motions, the maximum errors corresponding to the nonlinear stiffness model are slightly smaller than the ones corresponding to the constant stiffness model, and the difference is about 5–200 nm/nrad. During the working phases of scanning movements, the vibrations corresponding to the nonlinear stiffness model are larger than the ones corresponding to the constant stiffness model, and the difference is approximately 3–110 nm/nrad.

In the stepping movement and acceleration and deceleration phases of scanning movements, the slider is pushed by the driving forces, thus causing the aerostatic bearing groups fixed on it to deflect and shift in the supporting direction. The change in gas film thickness increases the total stiffness of the bearing groups depending on the nonlinear relationship between film thickness and bearing stiffness. Hence, the errors are reduced correspondingly. During the working phases of

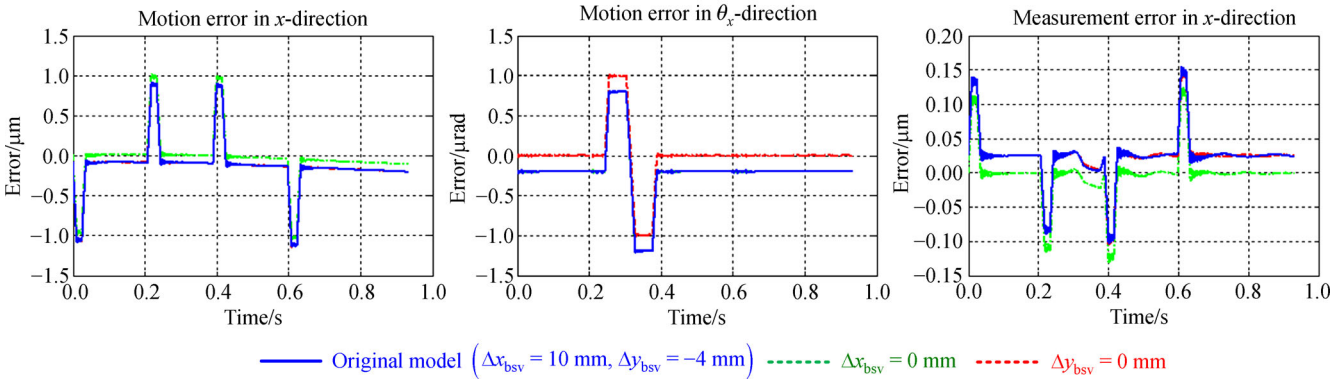

Fig. 10 Simulation results of the effects of Δx_{bsv} and Δy_{bsv} on dynamic errors

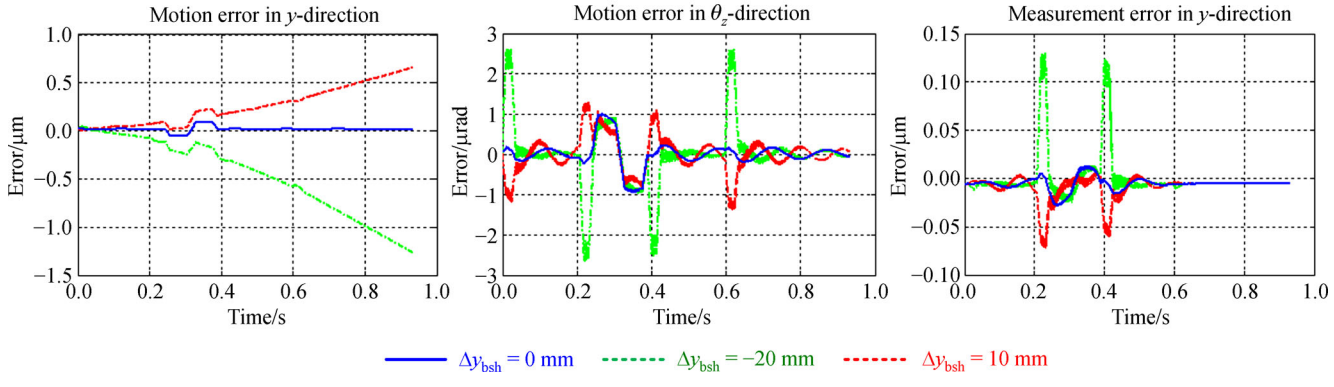

Fig. 11 Simulation results of the effects of Δy_{bsh} on dynamic errors

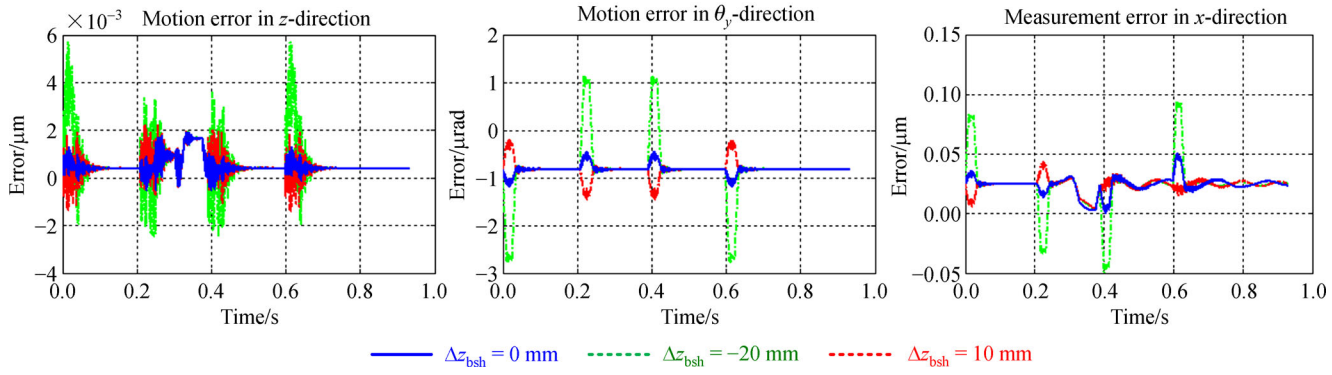

Fig. 12 Simulation results of the effects of Δz_{bsh} on dynamic errors

Table 2 Effects of the center point positions of aerostatic bearing groups on dynamic errors

Displacement of the center point	e_x	e_y	$e_{\theta z}$	e_z	$e_{\theta x}$	$e_{\theta y}$	$e_{\mathrm{m}x}$	$e_{\mathrm{m}y}$	$e_{\mathrm{m}\theta z}$
$\lvert\Delta x_{\mathrm{bsv}}\rvert\downarrow$	SB ↓			SB ↓, Scw ↓, Sca ↓ (Sca → min, when $\Delta x_{\mathrm{bsv}}\approx$10 mm)		SB ↓	SB ↓		SB ↓, St ↓
$\lvert\Delta y_{\mathrm{bsv}}\rvert\downarrow$		SB ↓		SB ↓, St ↓	SB ↓			SB ↓	SB ↓, Sca ↓, Scw ↓
$\lvert\Delta y_{\mathrm{bsh}}\rvert\downarrow$		PE ↓	Sca ↓, Scw ↓				($\Delta y_{\mathrm{bsh}}\downarrow$) Sca ↑	Sca ↓	
$\lvert\Delta z_{\mathrm{bsh}}\rvert\downarrow$				Sca ↓, Scw ↓		Sca ↓	Sca ↓	St ↑	Sca ↓

Table 3 Effects of the stiffness of aerostatic bearings on dynamic errors

Stiffness of aerostatic bearing	e_x	e_y	$e_{\theta z}$	e_z	$e_{\theta x}$	$e_{\theta y}$	$e_{\mathrm{m}x}$	$e_{\mathrm{m}y}$	$e_{\mathrm{m}\theta z}$
$K_{\mathrm{bsv}}\uparrow$	AL ↓	St ↓, SB ↓	Scw ↓	St ↓	St ↓, SB ↓	Sca ↓, Scw ↓, SB ↓	Sca ↓, Scw ↓, SB ↓	St ↓, SB ↓	SS ↓, SB ↓
$K_{\mathrm{bsh}}\uparrow$	AL ↓	PE ↓	SS ↓, SB ↓			Scw ↓	Scw ↓, St ↓	Scw ↓, St ↓	

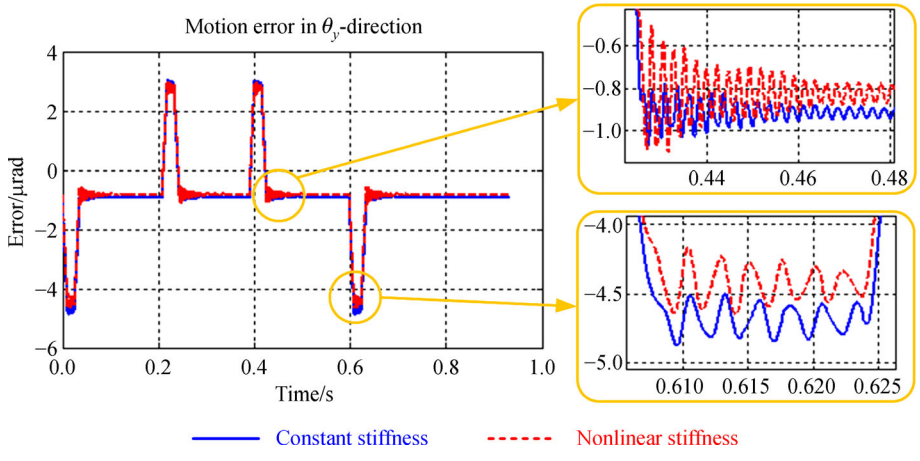

Fig. 13 Simulation results of motion errors corresponding to constant stiffness and nonlinear stiffness models

scanning movements, the vibrations of the beam and slider cause oscillations of gas film thickness. Thus, the bearing stiffness fluctuates constantly, thereby slowing the vibration attenuation.

If errors exist in preloading forces or initial film thicknesses, then the operating stiffness of aerostatic bearing groups will exhibit a large deviation from the rated value when the system reaches static balance. Thus,

the difference between the error results corresponding to the constant and nonlinear stiffness models will become more obvious than before, as shown in Figs. 14 and 15.

As shown in Fig. 16, even if the rated operating stiffness is the same, the system dynamic errors caused by different nonlinear stiffness characteristics may differ. The error results of Model 1 are close to the results of the constant model. Operating stiffness is not easily affected by the variation in gas film thickness when the rated operating stiffness is close to the maximum stiffness.

3.3 Influence of flatness errors of motion planes

3.3.1 Simulation setup

The effects of flatness errors of different motion planes on system dynamic errors are discussed in this section.

The *x*-*y* plane on the base is the one where AB_bb_v1, AB_bb_v2, and AB_bs_v move on, and its flatness error is identified as $e_{f\_bs\_xy}$. AB_bb_h moves on the *x*-direction guide plane fixed on the base, and the flatness error of the plane is identified as $e_{f\_bs\_x}$. The *y*-direction guide planes for AB_bs_h are on both sides of the beam, whose flatness error is identified as $e_{f\_bm\_y}$.

By setting the parameter values of the flatness error generator in the system dynamic accuracy model, multiple sets of values are assigned to $e_{f\_bs\_xy}$, $e_{f\_bs\_x}$, and $e_{f\_bm\_y}$ to simulate the system models with different flatness errors.

3.3.2 Results and discussion

If $e_{f\_bs\_x} \neq 0$, the aerostatic bearing group AB_bb_h will vibrate in *y*, *Rx*, and *Rz* directions. However, the vibrations

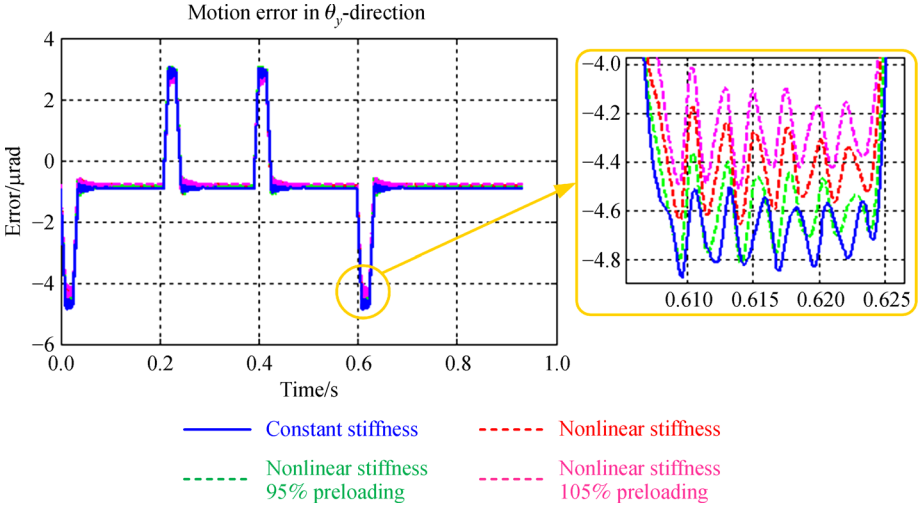

Fig. 14 Simulation results of motion errors corresponding to different preloading errors

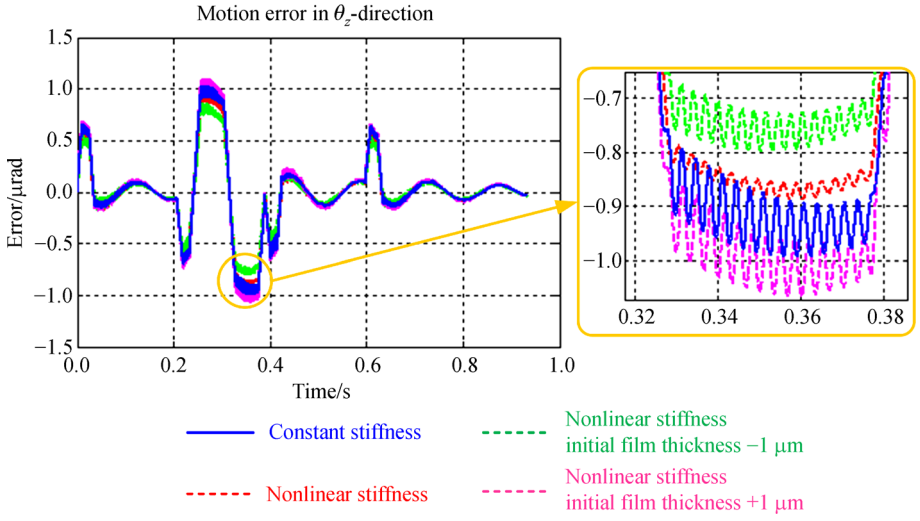

Fig. 15 Simulation results of motion errors corresponding to different initial film thickness errors

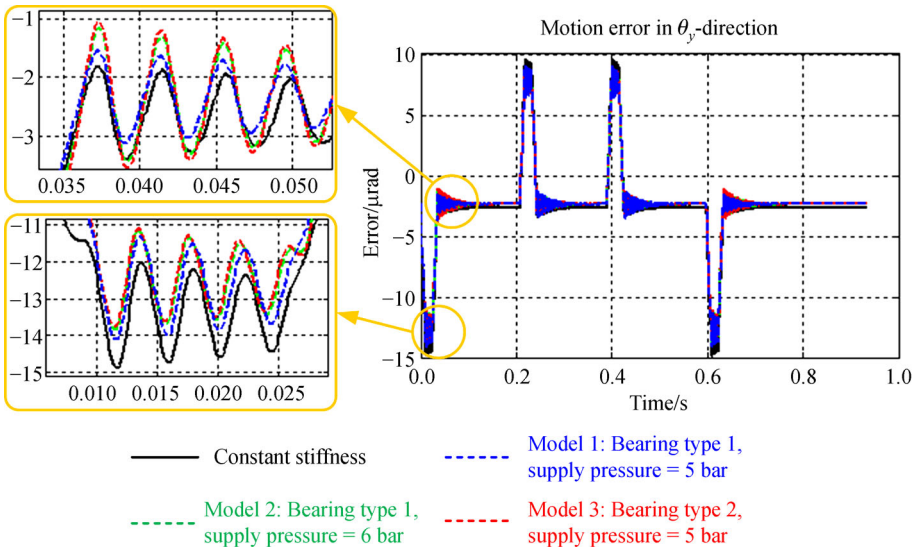

Fig. 16 Simulation results of motion errors corresponding to different nonlinear stiffness models. 1 bar = 10^5 Pa

will be isolated by the flexure hinges and the bearing group AB_bs_h and difficult to be transferred to the slider. Thus, $e_{f\_bs\_x}$ has little effect on the dynamic errors, as shown in Fig. 17. $e_{f\_bs\_xy}$ and $e_{f\_bm\_y}$ cause the vibrations of AB_bs_v and AB_bs_h, which directly affect the slider. Hence, $e_{f\_bs\_xy}$ and $e_{f\_bm\_y}$ have much greater effects on system errors than $e_{f\_bs\_x}$. The specific effects on dynamic errors are given in Table 4.

If the plane of motion is not flat, the variation amplitude of the gas film thickness of aerostatic bearings will be larger during system motion, and the influence of the nonlinear stiffness characteristic on the dynamic error will be more obvious. The difference between the maximum dynamic errors of the nonlinear stiffness and constant stiffness models is about 0.01–1.1 μm/μrad.

3.4 Influence of foundation vibrations

3.4.1 Simulation setup

System errors affected by foundation vibrations with different amplitudes are discussed in this section. By setting the parameter values of the foundation vibration generator, multiple sets of vibration signals, which are white noise excitations with diverse amplitudes, are generated. These vibration signals are applied to the base in the system accuracy model to simulate different foundation vibration conditions. In the system simulations, flatness errors are assumed to exist on all motion planes, that is, $e_{f\_bs\_xy}$, $e_{f\_bs\_x}$, and $e_{f\_bm\_y}$ are not equal to 0.

3.4.2 Results and discussion

The error simulation results of the system model with foundation vibrations and flatness errors on motion planes are illustrated in Fig. 18. The disturbances in *x*, *y*, and *Rz* directions caused by foundation vibrations cause the open-loop motion control to fail. The slider deviates from the predetermined trajectory and cannot stop accurately. The motion errors increase as the vibration amplitudes increase. Hence, foundation vibrations have a significant influence on the motions in *x*, *y*, and *Rz* directions. Compared with the flatness errors on motion planes, foundation vibrations have fewer effects on the motion errors in *z*, *Rx*, and *Ry* directions. One of the main reasons is that the stiffness of aerostatic bearing groups is large enough that the slider can quickly follow the vibration of the base. Thus, the relative displacements between the base and slider caused by the foundation vibrations are small. These relative displacements increase the variation of the gas film thickness of the aerostatic bearing group AB_bs_v, which makes the effects of the nonlinear stiffness characteristics of aerostatic bearings highly obvious. The difference between the maximum dynamic errors of the nonlinear stiffness and constant stiffness models is increased to 0.05–1.6 μm/μrad.

Table 4 Effects of flatness errors of motion planes on dynamic errors

Flatness error of motion plane	e_x	e_y	$e_{\theta z}$	e_z	$e_{\theta x}$	$e_{\theta y}$	e_{mx}	e_{my}	$e_{m\theta z}$
$e_{f\_bs\_xy}\downarrow$	SS ↓	SS ↓		SS ↓	SS ↓	SS ↓	SS ↓	SS ↓	SS ↓
$e_{f\_bm\_y}\downarrow$	St ↓, SB ↓, PE ↓	SS ↓	SS ↓				SS ↓	SS ↓	

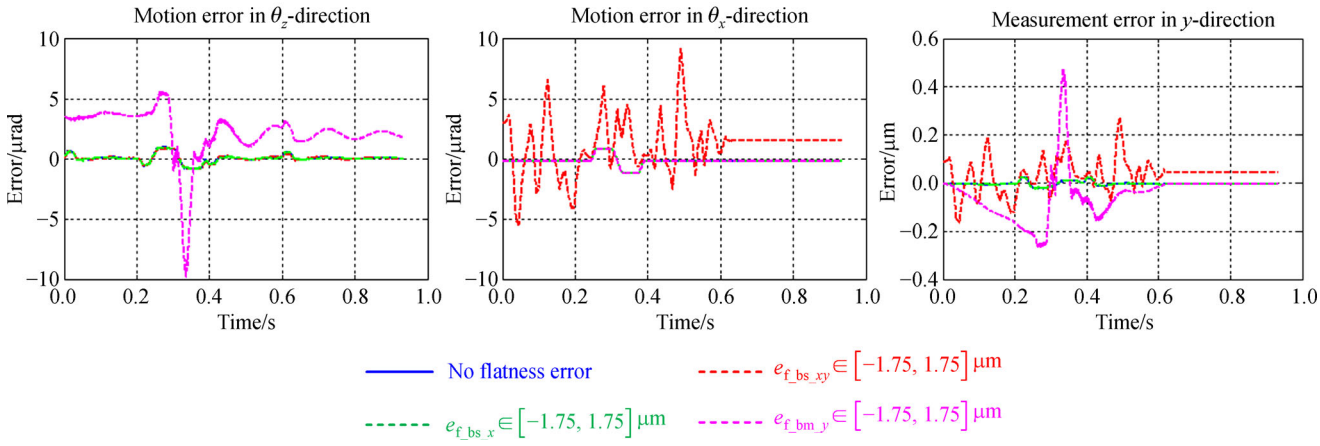

Fig. 17 Simulation results of dynamic errors corresponding to flatness errors on different planes

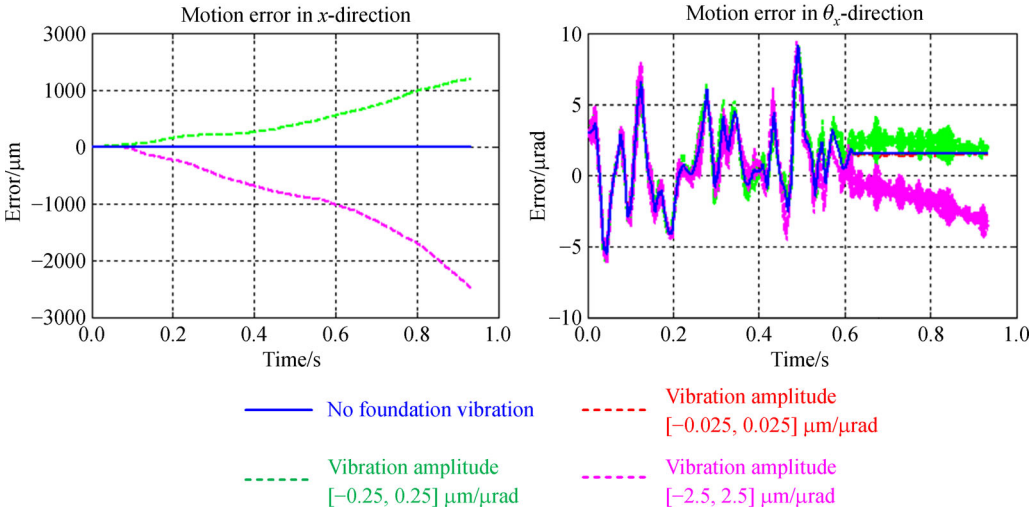

Fig. 18 Simulation results of dynamic errors affected by foundation vibrations with different amplitudes

4 Method encapsulation and application

The methods to establish the system dynamic accuracy model and quantitatively analyze the dynamic accuracy and influence of structural design factors are programmed and integrated into a prototype system of a software framework supporting the dynamic design of nano-precision positioning stages, as shown in Fig. 19. This work was performed to extend the application of the approach to other system instances and even other configurations.

A lot of parameterized model templates of the key components and modules in the system dynamic accuracy model have been developed based on the systematic modeling method. And these templates include dynamic topologies of H-type and other configurations, equivalent dynamic models of aerostatic bearings, single- and multi-axis interferometer measurement models, displacement solving algorithms corresponding to interferometers layouts, foundation vibration generators, flatness error generators, and driving signal generators. Instance models of the key components and modules can be rapidly generated by using the model templates and can then be used to assemble dynamic accuracy models for different system instances. On the basis of the assembled system model, the dynamic accuracy and influence of structural design factors can be easily analyzed by calling on the simulation scripts developed through the accuracy analysis method.

The prototype system was applied to the design of a stage used in a packaging lithography machine. The designed structural scheme of the stage was modeled using the model templates in the prototype system. The structural and dynamic design factors in the parameterized system model were modified to optimize the scheme. The installation position of linear motors and the selection

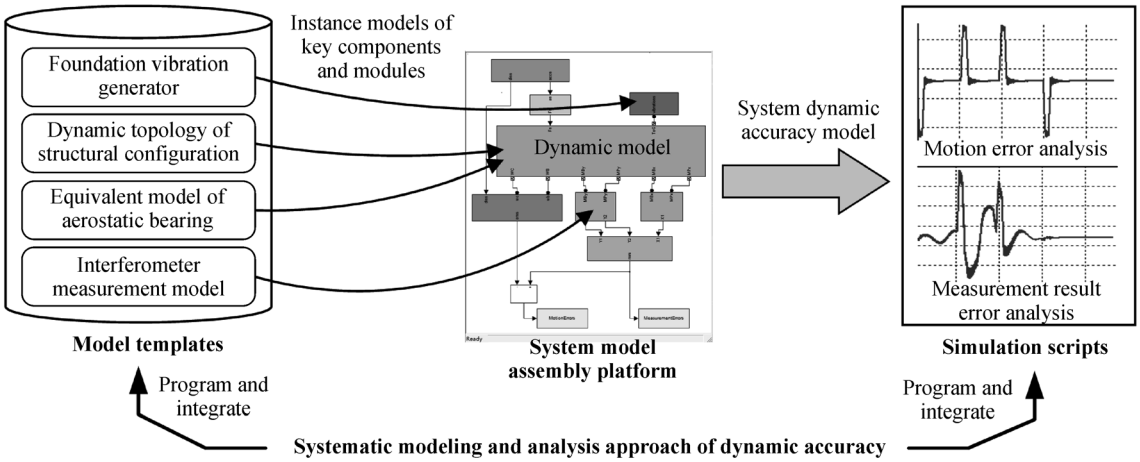

Fig. 19 Design framework supporting the dynamic design of nano-precision positioning stages

Table 5 Structural parameters in the original and optimized schemes

Scheme	Δz_{Fx} /mm	Δx_{Fy} /mm	Δx_{bsv} /mm	Δy_{bsv} /mm	Δy_{bsh} /mm	Bearing in AB_bs_h
Original	−17.8	10.5	10.2	−3.8	−3.8	Original bearing
Optimized	−5.0	5.0	5.0	−2.0	−2.0	Modified bearing

and layout of aerostatic bearings were modified, which have little impact on the structural design of other parts, as shown in Table 5. In the optimized structural scheme, the acting points of driving forces and the center points of aerostatic bearing groups were closer to the mass center of moving parts. The aerostatic bearing product applied in AB_bs_h was replaced with the one that can reach higher stiffness by slightly reducing the initial film thickness. The stiffness characteristics and rated operating stiffness of the modified bearing are shown in Fig. 20.

Without considering the motion plane error and the foundation vibration, the system model of the optimized scheme was simulated, and the positioning accuracy after completing a stepping motion was investigated. As shown in Table 6 and Fig. 21, the positioning accuracy was improved.

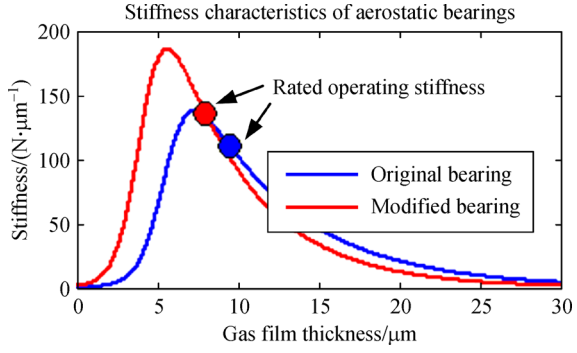

Fig. 20 Stiffness characteristics of the original and modified bearings

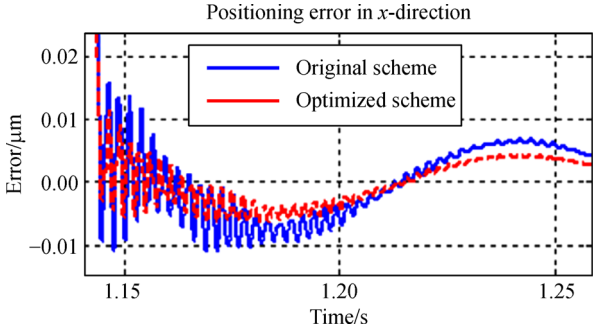

Fig. 21 Simulation results of positioning errors of the original and optimized schemes

Table 6 Simulation results of positioning errors of the original and optimized schemes

Scheme	Minimum/nm	Maximum/nm	Mean/nm	Standard deviation/nm
Original	−11.0	15.9	−1.1	5.8
Optimized	−6.4	11.4	−0.7	3.5

5 Conclusions

A parameterized system dynamic accuracy model of a nano-precision positioning stage is built. The system dynamic accuracy model integrates the multi-rigid-body dynamic model of the mechanical system and the interferometer measurement models and can simultaneously calculate the motion and measurement result errors of the operating point during system motion simulation. In the system accuracy model, the homogeneous transformation matrices of the plane mirrors with respect to the interferometers are used as the interfaces, through which the interferometer measurement models can be connected to the system dynamic model. In the system dynamic model, an aerostatic bearing is equivalently represented as a nonlinear spring whose acting point can slide on the motion plane. Richards model is employed to represent the nonlinear relationship between supporting force and gas film thickness, and the flatness error of the motion plane is considered.

Based on the system dynamic accuracy model, the effects of the structural design factors on the motion and measurement result errors are analyzed, including the positions of the driving force acting points and the center points of aerostatic bearing groups, the stiffness characteristics of aerostatic bearings, the flatness errors of motion planes, and the foundation vibrations. The analysis results indicate that for the $2+1$ layout 3-DOF interferometer measurement system, the measurement result errors in the controlled directions may reach tens of nanometers or nano-radians due to structural vibrations in the non-control directions. The acting point of the y-direction driving force and the center points of the aerostatic bearing groups fixed on the slider should be as close as possible to the mass center of the slider, which is an effective means to reduce system dynamic errors. When designing aerostatic bearings, the stiffness variation during system motion caused by the nonlinear stiffness characteristic of aerostatic bearing should be considered, together with the resulting effects on system dynamic errors.

The systematic modeling and analysis approach for dynamic accuracy are programmed as simulation scripts and parameterized model templates of key components and modules. They are integrated into a design framework supporting the dynamic design of nano-precision positioning stages. A stage used in a packaging lithography machine is designed with the help of the framework.

Acknowledgements This work was partially supported by the National Science and Technology Major Project of China (Grant Nos. 2009ZX02204-006 and 2017ZX02101007-002) and the National Natural Science Foundation of China (Grant Nos. 51435006 and 51675195).

References

1. ITRS. 2013 Edition, IRC Overview, International Technology Roadmap for Semiconductors
2. Torralba M, Valenzuela M, Yagüe-Fabra J A, et al. Large range nanopositioning stage design: A three-layer and two-stage platform. Measurement, 2016, 89: 55–71
3. Gao W, Kim S W, Bosse H, et al. Measurement technologies for precision positioning. CIRP Annals-Manufacturing Technology, 2015, 64(2): 773–796
4. Smith S T, Chetwynd D G. Foundations of Ultraprecision Mechanism Design. London: Taylor & Francis e-Library, 2005
5. Schmidt R M, Schitter G, Eijk J V. The Design of High Performance Mechatronics: High-Tech Functionality by Multidisciplinary System Integration. Amsterdam: Delft University Press, 2011
6. Huo D, Cheng K, Wardle F. Design of Precision Machines in Machining Dynamics: Fundamentals, Applications and Practices. London: Springer, 2009
7. Huo D, Cheng K. A dynamics-driven approach to the design of precision machine tools for micro-manufacturing and its implementation perspectives. Proceedings of the Institution of Mechanical Engineers. Part B, Journal of Engineering Manufacture, 2008, 222(1): 1–13
8. Huo D, Cheng K, Wardle F. A holistic integrated dynamic design and modelling approach applied to the development of ultraprecision micro-milling machines. International Journal of Machine Tools and Manufacture, 2010, 50(4): 335–343
9. Srivatsan V, Katz R, Dutta D, et al. Dynamic error characterization for non-contact dimensional inspection systems. Journal of Manufacturing Science and Engineering, 2008, 130(5): 051003
10. Chen D, Han J, Huo C, et al. Effect of gas slip on the behavior of the aerostatic guideway. Industrial Lubrication and Tribology, 2017, 69(4): 447–454
11. Li Y, Wu Y, Gong H, et al. Air bearing center cross gap of neutron stress spectrometer sample table support system. Frontiers of Mechanical Engineering, 2016, 11(4): 403–411
12. He X, Chen X. The dynamic analysis of the gas lubricated stage in optical lithography. International Journal of Advanced Manufacturing Technology, 2007, 32(9–10): 978–984
13. Chen X, Li Z. Model reduction techniques for dynamics analysis of ultra-precision linear stage. Frontiers of Mechanical Engineering, 2009, 4(1): 64–70
14. Bao X, Mao J. Dynamic modeling method for air bearings in ultra-precision positioning stages. Advances in Mechanical Engineering, 2016, 8(8): 1−9

15. Denkena B, Dahlmann D, Sassi N. Analysis of an ultra-precision positioning system and parametrization of its structural model for error compensation. Procedia CIRP, 2017, 62: 335–339
16. Li W, Li B, Yang J. Design and dynamic optimization of an ultra-precision micro grinding machine tool for flexible joint blade machining. International Journal of Advanced Manufacturing Technology, 2017, 93(9–12): 3135–3147
17. Kim K, Ahn D, Gweon D. Optimal design of a 1-rotational DOF flexure joint for a 3-DOF H-type stage. Mechatronics, 2012, 22(1): 24–32
18. Erkorkmaz K, Gorniak J M, Gordon D J. Precision machine tool *X-Y* stage utilizing a planar air bearing arrangement. CIRP Annals-Manufacturing Technology, 2010, 59(1): 425–428
19. Chen R, Yan L, Jiao Z, et al. Dynamic modeling and analysis of flexible H-type gantry stage. Journal of Sound and Vibration, 2019, 439: 144–155
20. Kilikevičius A, Kasparaitis A. Dynamic research of multi-body mechanical systems of angle measurement. International Journal of Precision Engineering and Manufacturing, 2017, 18(8): 1065–1073
21. Zhou B, Wang S, Fang C, et al. Geometric error modeling and compensation for five-axis CNC gear profile grinding machine tools. International Journal of Advanced Manufacturing Technology, 2017, 92(5–8): 2639–2652
22. Guo S, Jiang G, Mei X. Investigation of sensitivity analysis and compensation parameter optimization of geometric error for five-axis machine tool. International Journal of Advanced Manufacturing Technology, 2017, 93(9–12): 3229–3243
23. Chen J X, Lin S W, Zhou X L. A comprehensive error analysis method for the geometric error of multi-axis machine tool. International Journal of Machine Tools and Manufacture, 2016, 106: 56–66
24. Tian W, Gao W, Zhang D, et al. A general approach for error modeling of machine tools. International Journal of Machine Tools and Manufacture, 2014, 79: 17–23
25. Zhang Z, Liu Z, Cheng Q, et al. An approach of comprehensive error modeling and accuracy allocation for the improvement of reliability and optimization of cost of a multi-axis NC machine tool. International Journal of Advanced Manufacturing Technology, 2017, 89(1–4): 561–579
26. Cheng Q, Zhang Z, Zhang G, et al. Geometric accuracy allocation for multi-axis CNC machine tools based on sensitivity analysis and reliability theory. Proceedings of the Institution of Mechanical Engineers. Part C, Journal of Mechanical Engineering Science, 2015, 229(6): 1134–1149
27. Liu Y, Yuan M, Cao J, et al. Evaluation of measurement uncertainty in H-drive stage during high acceleration based on Monte Carlo method. International Journal of Machine Tools and Manufacture, 2015, 93: 1–9
28. Gao Z, Hu J, Zhu Y, et al. The research on geometric error's tolerance design of *X-Y* stage's measurement system accuracy. Transactions of the Institute of Measurement and Control, 2013, 35(5): 672–682
29. Gao Z, Hu J, Zhu Y, et al. A new 6-degree-of-freedom measurement method of *X-Y* stages based on additional information. Precision Engineering, 2013, 37(3): 606–620
30. Du S, Hu J, Zhu Y, et al. Analysis and compensation of synchronous measurement error for multi-channel laser interferometer. Measurement Science and Technology, 2017, 28(5): 055201
31. Teng W, Zhou Y F, Mu H H, et al. An algorithm on laser measurement model of ultra-precision motion stage and error compensation. China Mechanical Engineering, 2009, 20(12): 1492–1497 (in Chinese)
32. Wen X, Zhou Y F, Mu H H, et al. An algorithm for the compensation of geometrical error in laser interferometer measurement. Machinery Design & Manufacture, 2011, (9): 46–48 (in Chinese)
33. Liu C, Pu Y, Chen Y, et al. Design of a measurement system for simultaneously measuring six-degree-of-freedom geometric errors of a long linear stage. Sensors, 2018, 18(11): 3875
34. Liang C Y, Luo X, Chen X D. Generating equivalent models of aerostatic bearings for precise positioning stage design in a knowledge-based framework. In: Proceedings of 2015 Advanced Design Concepts and Practice. Lancaster: Destech Publications, 2016, 138–148
35. Chen X D, Zhu J C, Chen H. Dynamic characteristics of ultra-precision aerostatic bearings. Advances in Manufacturing, 2013, 1(1): 82–86
36. Agilent Technologies. Agilent Laser and Optics User's Manual, Volume II. 2007
37. Fan K C, Chen M J A. 6-degree-of-freedom measurement system for the accuracy of *X-Y* stages. Precision Engineering, 2000, 24(1): 15–23